

A New Comprehensive X-ray Spectral Model from the Post-shock Accretion Column in Intermediate Polars

Takayuki Hayashi^{1,2} * and Manabu Ishida^{1,2}

¹*The Institute of Space and Astronautical Science/JAXA, 3-1-1 Yoshinodai, Chuo-ku, Sagami-hara 252-5210*

²*Department of Physics, Tokyo Metropolitan University, 1-1 Minami-Osawa, Hachioji, Tokyo 192-0397*

ABSTRACT

We model the post-shock accretion column (PSAC) of intermediate polars (IPs) with the specific accretion rate being floated in the range between 0.0001 and $100 \text{ g cm}^{-2} \text{ s}^{-1}$ and the metal abundance in the range between 0.1 and 2 times of the solar, and taking into account the gravitational potential with radial dependence, non-equipartition between ions and electrons, and ionization non-equilibrium. We fully take into account the dipole geometry for the PSAC. The specific accretion rate significantly affects the structure of the PSAC, and there is a critical rate below which the profiles of the density and temperature distributions deviate from those of the standard model. This happens when the specific accretion rate is 1 and $30 \text{ g cm}^{-2} \text{ s}^{-1}$ for the 0.7 and $1.2 M_{\odot}$ white dwarf (WD), respectively, or the height of the PSAC becomes 1% of the white dwarf radius. Below the critical specific accretion rate, the present standard model is no longer valid. We calculate the spectra of the PSACs with the density and temperature distributions described above. Input parameters are the mass of the WD, the specific accretion rate, and the metal abundance. The spectral shape is constant and consistent with that of the standard model if the specific accretion rate is larger than the critical value, except for density-dependent emission lines. Below the critical specific accretion rate, on the other hand, the spectra soften as the specific accretion rate decreases. Associated with this, the maximum temperature of the PSAC becomes significantly lower than that of the standard model below the critical specific accretion rate. Although the ionization non-equilibrium are also considered in the spectral calculation, the effects are limited because the radiation from ionization non-equilibrium plasma is a few percent of the whole at most.

Key words: accretion, accretion discs – methods: data analysis – fundamental parameters – novae, cataclysmic variables – white dwarfs – X-rays: stars.

1 INTRODUCTION

Magnetic cataclysmic variables (mCVs) are binary systems made up of a Roche Lobe-filling late type star and a magnetized ($B > 0.1 \text{ MG}$) white dwarf (WD). There are two subclasses in the mCV. One is the polar in which the magnetic field of the WD is so strong ($B > 10 \text{ MG}$) that the WD rotation and the binary motion are synchronized. The other is the intermediate polar (IP), the subject of this paper, where the WD rotation is not synchronized with the binary revolution. In IPs, matter split over the Roche lobe of the secondary star initially forms an accretion disk, is funneled by the strong magnetic field within the Alfvén radius, and falls toward the WD surface nearly at the free fall velocity. Since the accreting matter becomes highly supersonic as it descends along the magnetic field line, a strong shock is

formed and the matter is heated up to a temperature of order 10 keV . The high temperature plasma formed below the shock front is cooled via optically thin thermal plasma emission, and finally settles onto the WD surface. The plasma flow in the downstream side of the shock is called the post-shock accretion column (PSAC). X-ray spectra emitted from the IPs reflect structure of the PSAC such as radial distributions of the temperature and density. One of the most important parameter is the maximum temperature (T_{max}) of the plasma. Since this quantity reflects the depth of the gravitational potential of the WD ($\propto M_{\text{WD}}/R_{\text{WD}}$), the WD mass can be estimated from the X-ray spectra with the aid of a theoretical WD mass-radius relation, for example, described by Nauenberg (1972),

$$R_{\text{WD}} = 7.8 \times 10^8 \left[\left(\frac{1.44 M_{\odot}}{M_{\text{WD}}} \right)^{2/3} - \left(\frac{M_{\text{WD}}}{1.44 M_{\odot}} \right)^{2/3} \right]^{1/2} \text{ cm.} \quad (1)$$

* E-mail: thayashi@astro.isas.jaxa.jp

Hōshi (1973) first considered a steady and spherically symmetric accretion flow onto WDs. He discussed that near the WD surface a shock is formed and a hot plasma between the shock front and the WD surface emits thermal radiation. Although he simply carried out arithmetic operations, he estimated some physical quantities, for example, an effective temperature and emission measure of the post-shock plasma. Shortly after Hōshi (1973), Aizu (1973) analytically calculated the distributions of the temperature and the density along the plasma flow under the assumption that the thickness of the emission region, which corresponds to the height of the PSAC, is negligible compared with the WD radius. This assumption means that the gravitational potential can be considered as constant throughout the PSAC. Since his assumption appeared to be reasonable for high accretion rate systems and the analytically expressed temperature and density distributions are easily accommodated to the observed spectra, Aizu model had been used for evaluation of the observed spectra and WD mass estimation until a few tens of years after his publication, for example, in Fujimoto & Ishida (1997).

After that, a lot of theoretical studies were performed for the PSAC (e.g. Imamura & Durisen 1983, Woelk & Beuermann 1996, Canalle et al. 2005, Saxton et al. 2005 and Saxton et al. 2007). They included two-fluid effects, Compton cooling, effect of gravitational potential or dipolar geometry. Their calculations are, however, too complex to be applied to observed X-ray spectra. Wu, Chanmugam, & Shaviv (1994) and Cropper, Ramsay, & Wu (1998), on the other hand, beautifully simplified the PSAC model formulation, which enables us to use it for evaluating the observed spectra, and to extract information of the PSAC and the WD. They assumed one-temperature (i.e. equipartition between ions and electrons), one-dimensional and cylindrical geometry for the PSAC. Cropper et al. (1999) continued along the path of improvements to that technique by addressing the elimination of a negligible shock height assumption. In so doing, they explored and elucidated clearly for the first time the effects of including a radially varying gravitational potential along the PSAC. The model of Cropper et al. (1999) have been used for the recent WD mass measurements with X-ray spectra (Ramsay et al. 2000, Suleimanov, Revnivtsev, & Ritter 2005, Brunschweiler et al. 2009, Yuasa et al. 2010 and so on) and is said to be the present standard model of the PSAC. In fact, the standard model can reproduce observed spectra well.

While Cropper et al. (1999) considered the radially varying-gravitational potential, they hardly discussed the difference of the mass accretion rate per unit area called "specific accretion rate". Moreover, some studies using the standard model (e.g. Suleimanov, Revnivtsev, & Ritter 2005 and Yuasa et al. 2010 for light WDs) noted that the PSAC structure is not influenced so much, and hence the WD masses estimated with the observed spectra are altered by the specific accretion rate only a little. As a matter of fact, Yuasa et al. (2010) investigated the influence of the specific accretion rate a on the WD mass estimation in the range $a = 0.1\text{--}10 \text{ g cm}^{-2} \text{ s}^{-1}$. As a results, they showed that the estimated WD mass is affected by less than $\sim 30\%$ for a WD less massive than $1.2 M_{\odot}$ where most WDs are likely to belong.

However, some observations suggest that the specific accretion rate distributes in a wider range. For instance, the accretion rate of AE Aquarii and V1223 Sagittarii are estimated at $\dot{M} \sim 10^{14} \text{ g s}^{-1}$ (Eracleous, Halpern, & Patterson 1991) and $8.4 \times 10^{16} \text{ g s}^{-1}$ (Hayashi et al. 2011) with the standard model, respectively. Furthermore, Cropper, Ramsay, & Wu (1998) obtained the specific accretion rate of EX Hydrae of $0.001 \text{ g cm}^{-2} \text{ s}^{-1}$ as the best fit parameter, which is three orders of magnitude lower than that assumed in the standard model, although they did not take into account the radially varying-gravitational potential. Although these results are indirect evaluations, they suggest the specific accretion rate may be different by more than a few orders magnitudes among the IPs.

One of the remaining major issues of the standard model is that the mass of the WD and the height of PSAC in some IPs evaluated by the standard model are inconsistent with that derived from observations in low accretion rate or massive WD systems. The maximum temperature of the plasma in the peculiar IP AE Aquarii is 4.6 keV (Itoh et al. 2006). Based on the standard model, the low maximum temperature means that the WD of the AE Aquarii is no more massive than $0.2 M_{\odot}$ (see figure 2 in Yuasa et al. 2010), which is only one-fourth of the $0.79 M_{\odot}$ measured with the line Doppler measurement in optical band (Casares et al. 1996). In this system, owing to its fast WD spin with a period of ~ 33 sec (Patterson 1979), the propeller effect plays an important roll and blows away most of the accreting matter (Wynn, King, & Horne 1997), which leads very low mass accretion rate $\dot{M} \sim 10^{14} \text{ g s}^{-1}$. The WD mass of EX Hydrae, $0.42 \pm 0.02 M_{\odot}$ (Yuasa et al. 2010) estimated with the standard model contradicts the optical measurement $0.79 \pm 0.26 M_{\odot}$ (Beuermann & Reinsch 2008). We believe that the latter measurement is fairly reliable because EX Hydrae is a double-lined eclipsing IP. This system is also a low accretion-system, $\dot{M} = 2.8 \times 10^{15} \text{ g s}^{-1}$ (Suleimanov, Revnivtsev, & Ritter 2005). The WD mass of a nova IP GK Perseus is estimated at $1.15 M_{\odot}$ with "nova universal decline law" (Hachisu & Kato 2007), which is much greater than the X-ray estimations, $0.59 \pm 0.05 M_{\odot}$ by Suleimanov, Revnivtsev, & Ritter (2005), $0.90 \pm 0.12 M_{\odot}$ by Brunschweiler et al. (2009) and $0.92^{+0.39}_{-0.13} M_{\odot}$ by Landi et al. (2009). Although this IP is very high accretion-rate system of $81.5 \times 10^{16} \text{ g s}^{-1}$, the massive WD (Suleimanov, Revnivtsev, & Ritter 2005) causes a relatively large error in the mass estimation. As for the height of the PSAC in EX Hydrae, the standard model expects about 2×10^6 cm, comparable to 0.2% of the WD radius (Yuasa et al. 2010), Allan, Hellier, & Beardmore (1998) derived the height as tall as the WD radius. These discrepancies show that the standard model should further be improved in some cases, especially for the cases of the lower specific accretion rate and of the massive WD.

In order to resolve the issues described above, we modify the standard model in the following four points; (1) the specific accretion rate, which is fixed at $1 \text{ g cm}^{-2} \text{ s}^{-1}$ in the standard model, is floated in the wide range from 0.0001 to $100 \text{ g cm}^{-2} \text{ s}^{-1}$. The lower specific accretion rate enhances the height of the PSAC because the density becomes lower, which results in a longer cooling time. The PSAC extension further requires; (2) the dipole should be considered as the PSAC geometry instead of the cylinder used in the standard

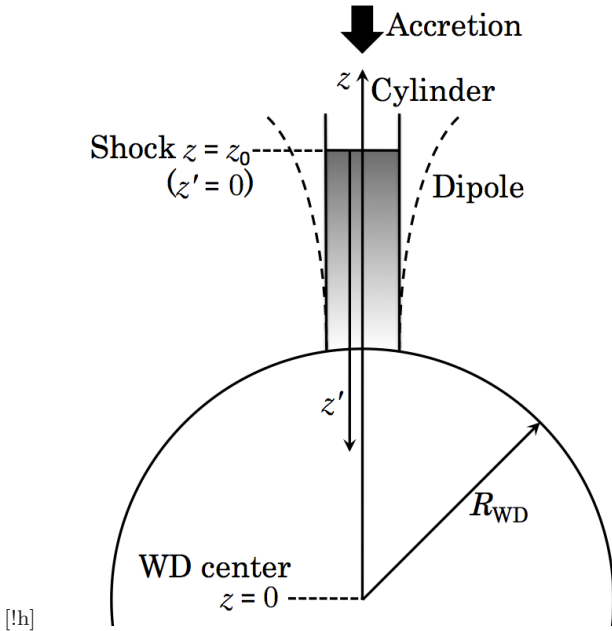


Figure 1. Geometries of the PSAC models. Dashed lines show the dipolar geometry.

model, which reduces the density further because of the funnel shape of the PSAC. Due to the density reduction; (3) the non-equilibrium between ions and electrons and (4) the ionization non-equilibrium should be taken into account which are not considered in the standard model. These modifications are more important for the IPs holding the massive WD because the more massive WD is smaller in size and the PSAC height becomes more significant compared with the WD radius at a higher specific accretion rate.

This paper is organized as follows. The calculation scheme is described in section 2. In section 3, we investigate the PSAC structure at various specific accretion rate and metal abundance. In section 4, the spectra emitted from the PSACs are shown and their dependence on the WD mass, the specific accretion rate and the metal abundance are discussed. Finally, we summarize our results in section 5.

2 MODELING THE POST-SHOCK ACCRETION COLUMN

We modeled the PSAC according to the guidelines described in the previous section. Following the method of Cropper et al. (1999) and Suleimanov, Revnivtsev, & Ritter (2005), the distributions of the density and temperature were calculated. The simultaneous differential equation involving the mass continuity equation

$$\frac{d}{dz}(\rho v S) = 0, \quad (2)$$

the momentum equation

$$\frac{d}{dz}(\rho v^2 + P) = -\frac{GM_{\text{WD}}}{z^2}\rho - \frac{\rho v^2}{S} \frac{dS}{dz}, \quad (3)$$

the energy equation

$$v \frac{dP}{dz} + \gamma P \frac{dv}{dz} = -(\gamma - 1) \left(\varepsilon - \frac{\rho v^3}{2S} \frac{dS}{dz} \right) \quad (4)$$

and the ideal-gas law

$$P = \frac{\rho k T}{\mu m_{\text{H}}} \quad (5)$$

describes the PSAC structure. Here, z is the spatial coordinate shown in figure 1 whose origin is the WD center, v is the bulk velocity, ρ is the mass density, T is the averaged temperature, P is the thermal pressure of the plasma, $\gamma = 5/3$ is the adiabatic index, and $\mu = 0.62$ is the mean molecular weight. S is the cross-section of the PSAC and assumed to be proportional to a power law function of z ,

$$S \propto z^n. \quad (6)$$

The power-law index n of 0 and 3 correspond to cylinder and dipole, respectively. ε is the cooling rate via optically thin thermal radiation given by

$$\varepsilon = \left(\frac{\rho}{\mu m_{\text{H}}} \right)^2 \Lambda(T), \quad (7)$$

where Λ is the cooling function. We adopt the Collisional Ionization Equilibrium (CIE) cooling function calculated by SPEX package (Schure et al. 2009). One may doubt that we should use a cooling function that reflects the non-equilibrium effects correctly. However, the part of the PSAC where the equipartition between the electron and the ion is not achieved is of lower density by a few orders of magnitude than that in the equilibrium part, and hence we can use the CIE cooling function throughout the PSAC. In fact, we substituted the emissivity of thermal bremsstrahlung for the CIE cooling function in the part where the electron temperature is below 90, 95, 99 and 99.9% of the averaged temperature. As a results, all these hybrid cooling functions gave nearly identical results. The second term of the right-hand side of the equation 3 describes the conversion of thermal energy into the kinematic energy in the PSAC because of decreasing cross-section as the Venturi nozzle.

The integral of equation (2) is

$$\rho v S = a S = a(4\pi R_{\text{WD}}^2 f) = \dot{M}, \quad (8)$$

where a is the mass accretion rate per unit area or "specific accretion rate" at the WD surface. f and \dot{M} are fractional accretion area and the mass accretion rate. In the standard model, $a = 1 \text{ g cm}^{-2} \text{ s}^{-1}$ and $n = 0$ for any IPs.

Equations (3) and (4) can be transformed with a and $z' = z_0 - z$, where z_0 is the shock coordinate (see figure 1),

$$\frac{dv}{dz'} = g(z') \frac{1}{v} - \frac{1}{a} \frac{dP}{dz'}, \quad (9)$$

$$\frac{dP}{dz'} = \frac{(\gamma - 1) \left(\varepsilon - \frac{\rho v^3}{2S} \frac{dS}{dz'} \right) a + g(z') \gamma P \rho}{\gamma P - av}, \quad (10)$$

where

$$g(z') = \frac{GM_{\text{WD}}}{(z_0 - z')^2}. \quad (11)$$

Equations (9) and (10) were solved from the top of the PSAC, $z = z_0 (z' = 0)$ to WD surface, $z = R_{\text{WD}} (z' =$

$z_0 - R_{\text{WD}}$) with the following boundary conditions at $z = z_0$ assuming the strong shock at the top of the PSAC,

$$v_0 = 0.25\sqrt{2GM_{\text{WD}}/z_0} \quad (12)$$

$$\rho_0 = \frac{a}{v_0}, \quad (13)$$

$$P_0 = 3av_0, \quad (14)$$

$$T_0 = 3\frac{\mu m_{\text{H}}}{k}v_0^2 \quad (15)$$

and soft landing,

$$v_{\text{WD}} = 0 \text{ (at WD surface)}. \quad (16)$$

The boundary conditions are uniquely given by specifying M_{WD} , a , and z_0 . Of them, the shock position z_0 matching the boundary conditions was found by iteration (shooting method). In so doing, we utilize the mass-radius relation of WDs given by equation 1.

Unlike the standard model, we consider non-equipartition between ions and electrons. After ions are immediately heated up by the strong shock, electrons are heated by Coulomb scattering with the ions. Time variation of the electron temperature is written as

$$\frac{dT_e}{dt} = \frac{T_i - T_e}{t_{\text{eq}}}, \quad (17)$$

where t_{eq} is the time scale of equipartition calculated with

$$t_{\text{eq}} = 5.87 \frac{A_e A_i}{n_i \text{ cm}^{-3} Z_e^2 Z_i^2 \ln \Lambda} \left(\frac{T_i \text{ K}}{A_i} + \frac{T_e \text{ K}}{A_e} \right)^{3/2} \text{ s}. \quad (18)$$

(Spitzer 1962). Here, T (in Kelvin), A and Z are temperature, atomic weight and charge, and subscript e and i imply electron and ion, respectively. n_i is the number density of the ion in a unit of cm^{-3} . For practical calculation, we followed the method of Wong & Sarazin (2009) in which eq.(17) can be rewritten as

$$\frac{d\tau}{dt} = \frac{2 \ln \Lambda}{503} \left\langle \frac{Z_i^2}{A_i} \right\rangle \frac{n}{T^{3/2} \tau^{-3/2} (1 - \tau)} \text{ s}^{-1} \quad (19)$$

where T is the averaged temperature;

$$T = \frac{n_e T_e + n_i T_i}{n_e + n_i} \quad (20)$$

and τ is relative electron temperature,

$$\tau \equiv \frac{T_e}{T}. \quad (21)$$

$\ln \Lambda$ is the Coulomb logarithm and can be approximated as

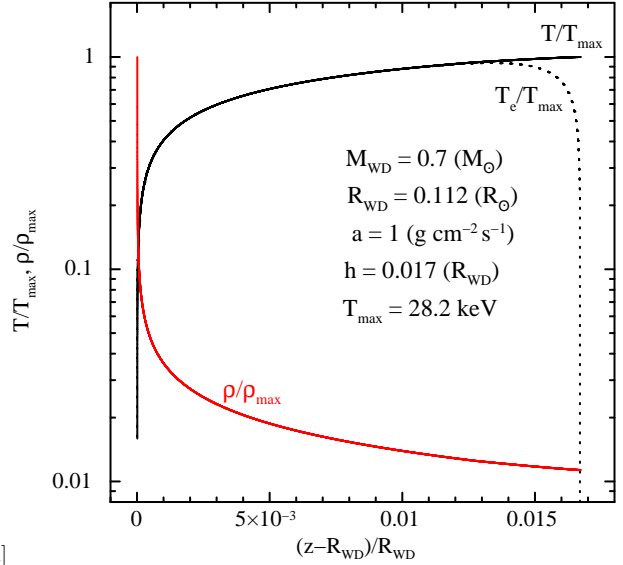
$$\ln \Lambda \sim 15.9 + \ln \left(\frac{T_e}{10^8 \text{ K}} \right) - \ln \left(\frac{n_e}{10^{16} \text{ cm}^{-3}} \right)^{1/2}. \quad (22)$$

The ionization of heavy element proceeds by impacts of electrons heated up by the interaction with the ions. Therefore, the ionization temperature trails the electron temperature. The angle bracket term is the mean value of the ratio of the square of ion charge and the atomic number, which equals 1 for our model of a pure hydrogen and helium gas. We set $A_e = 1/1836$.

3 CALCULATION RESULTS

3.1 Consistency with Previous Works

Figure 2 shows the temperature and density distributions of the cylindrical PSAC in the case of $a = 1 \text{ g cm}^{-2} \text{ s}^{-1}$,



[!h]

Figure 2. Averaged temperature (black solid line), electron temperature (black dotted line) and density (red solid line) distributions of a cylindrical PSAC for an IP of $M_{\odot} = 0.7 M_{\odot}$ and $a = 1 \text{ g cm}^{-2} \text{ s}^{-1}$. The parameters are common to figure 2 of Suleimanov, Revnivtsev, & Ritter (2005) and figure 3 of Yuasa et al. (2010).

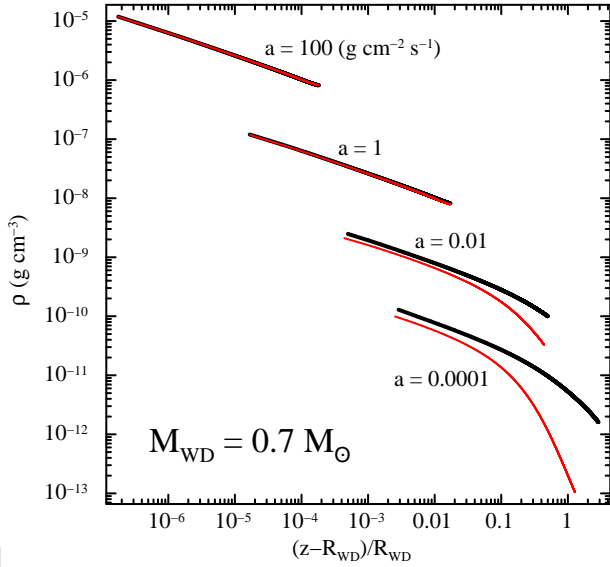
$M = 0.7 M_{\odot}$, and $Z = Z_{\odot}$. The temperature is normalized by their maximum values. The density, on the other hand, is normalized at a point one thousandth of the PSAC height, since it diverges at the WD surface. The profiles of these distributions closely resemble those from the previous studies of Suleimanov, Revnivtsev, & Ritter (2005) and Yuasa et al. (2010). Moreover, the shock height of our calculation is $0.017 R_{\text{WD}}$, which is close to that of Suleimanov, Revnivtsev, & Ritter (2005), $0.018 R_{\text{WD}}$ and Yuasa et al. (2010), $0.013 R_{\text{WD}}$. The electron temperature does not catch up the averaged temperature in the top of 20% of the PSAC. However, the density of that region is low. This suggests that the effect of non-equipartition between ions and electrons on the X-ray spectrum is limited.

3.2 Dependency on the specific accretion rate

We investigated influence of the specific accretion rate, which was fixed at $a = 1 \text{ g cm}^{-2} \text{ s}^{-1}$ in the standard model, on the PSAC structure in the range between 0.0001 and $100 \text{ g cm}^{-2} \text{ s}^{-1}$.

3.2.1 Density distribution and critical specific accretion rate

Figure 3 shows the density distributions of the cylindrical and dipolar PSAC with the specific accretion rate in the case of $M_{\text{WD}} = 0.7 M_{\odot}$ of 0.0001 , 0.01 , 1 and $100 \text{ g cm}^{-2} \text{ s}^{-1}$. In this figure, the right ends of each profile corresponds to the shock front. The other ends are terminated at 0.1% of a PSAC height of each case. This figure means that the PSAC becomes taller with a lower specific accretion rate due to a longer cooling time. When the specific accretion rate is suf-



[!h]

Figure 3. Density distributions of the cylindrical (black) and dipolar (red) PSACs for the WD mass of $0.7 M_{\odot}$ and a of 0.0001, 0.01, 1, $100 \text{ g cm}^{-2} \text{ s}^{-1}$. The right ends of the distributions correspond to the tops of the PSACs. The other ends are terminated at 0.1% of the PSAC height.

ficiently high ($a \gtrsim 1 \text{ g cm}^{-2} \text{ s}^{-1}$ for the $0.7 M_{\odot}$ WD), the density increases toward the WD surface with a power-law function of the distance from the WD surface, and its profile agrees between the dipolar and cylindrical geometries. On the other hand, when the specific accretion rate is sufficiently low ($a \ll 1 \text{ g cm}^{-2} \text{ s}^{-1}$ for the $0.7 M_{\odot}$ WD) the density distribution deviates from the power law. At the same time, the density distributions of the dipolar PSACs become different from those of the cylindrical because the difference between the two geometries emerges when the PSAC extends upwards and becomes compatible with the WD radius. We hereafter refer to the specific accretion rate below which the density profile of the cylindrical PSAC starts to deviate from that of the dipolar PSAC as the critical specific accretion rate a_{crit} . This definition of a_{crit} implies that the standard model is no longer valid in the regime $a < a_{\text{crit}}$. We systematically investigated a_{crit} as a function of the WD mass and found that $a = a_{\text{crit}}$ occurs when the PSAC height $\simeq 0.01 R_{\text{WD}}$, irrespective of the WD mass; for instance it is 1 and $30 \text{ g cm}^{-2} \text{ s}^{-1}$ for the 0.7 and $1.2 M_{\odot}$ WD, respectively. We refer to the readers to consult figure. 5 to find a_{crit} for a WD with any given mass.

3.2.2 Temperature distribution

The distributions of the averaged and electron temperature are shown in figure 4. Like the density distributions, the shapes of the temperature distributions agree between the geometries if $a \gtrsim a_{\text{crit}}$. If, on the other hand, $a \ll a_{\text{crit}}$, the averaged temperature reduces from that of the standard model over the whole PSAC and its distribution flattens. Although the averaged temperature monotonically decreases toward the WD surface in the standard model, that of our cylindrical PSAC, drawn with black color in figure 4, shows a peak in the middle of the PSAC at low enough specific

accretion rate. This is because energy input by gravity overcomes cooling energy loss since the low density reduces the cooling rate, and the tall PSAC retains larger amount of gravitational energy to be released below the shock front. For the dipolar cases, on the other hand, the temperature decrease is even faster than the cylindrical. This happens whenever a cross section of a subsonic flow shrinks along the streamline, such as the Venturi nozzle. In such a case, the bulk velocity of the flow increases at the expense of the thermal energy, which reduces the temperature. The averaged temperature of the dipolar PSAC monotonically decreases as the flow descends the PSAC for the $0.7 M_{\odot}$ WD throughout the range $a = 0.0001 - 100 \text{ g cm}^{-2} \text{ s}^{-1}$ unlike the cylindrical case. However, that of the $1.2 M_{\odot}$ WD shows a local minimum in the middle of the PSAC, as shown in the bottom right panel of figure 4. The heat transfer from the ion to the electron becomes slower with a lower density. At a very low specific accretion rate such as $0.0001 \text{ g cm}^{-2} \text{ s}^{-1}$ the non-equipartition area extends over the 80% region of the PSAC.

3.2.3 PSAC height

Relations between the height of the PSAC and the specific accretion rate are shown in figure 5 for the 0.4 , 0.7 and $1.2 M_{\odot}$ WDs. The PSAC constantly extends upwards with the lower specific accretion rate, but the slope of the PSAC height abruptly changes at a certain value of a . At around the high end of a , the height is proportional to a^{-1} , and the height of the PSAC is almost identical between the two, PSAC geometries, whereas at around the low end of a the heights are in proportion to $a^{-0.3}$ and $a^{-0.15}$ for the cylindrical and dipolar PSACs, respectively. It is interesting to note that the transition between these two regimes occurs at the PSAC height of about $0.2 R_{\text{WD}}$ for any mass of the WDs. The transition appears in larger specific accretion rate for a more massive WD, because the PSAC height easily becomes significant relative to WD radius due to its small radius. The radial extent of the PSAC can be as large as the WD radius in the lower specific accretion rate, which may resolve the problem about the observed PSAC height referred section 1.

3.2.4 Maximum temperature

The maximum temperature of electrons and that averaged over ions and electrons are shown as a function of the specific accretion rate in figure 6 for the 0.4 , 0.7 and $1.2 M_{\odot}$ WDs. The maximum temperature is indicative of the mass of the WD. In the region $a \gtrsim a_{\text{crit}}$, the maximum temperatures of the two geometries are identical and constant, as is predicted by the standard model. Below the a_{crit} , on the other hand, the maximum temperatures differ between the two geometries. In the dipolar geometry, the decrease of the maximum averaged temperature associated with the decrease of the specific accretion rate is faster than that in the cylindrical case. This is because the averaged temperature monotonically decrease for the dipolar PSAC while the hottest region emerges in the middle of the PSAC in the cylindrical geometry, as shown in the bottom four panels of figure 4. The electron maximum temperature reduces also faster for

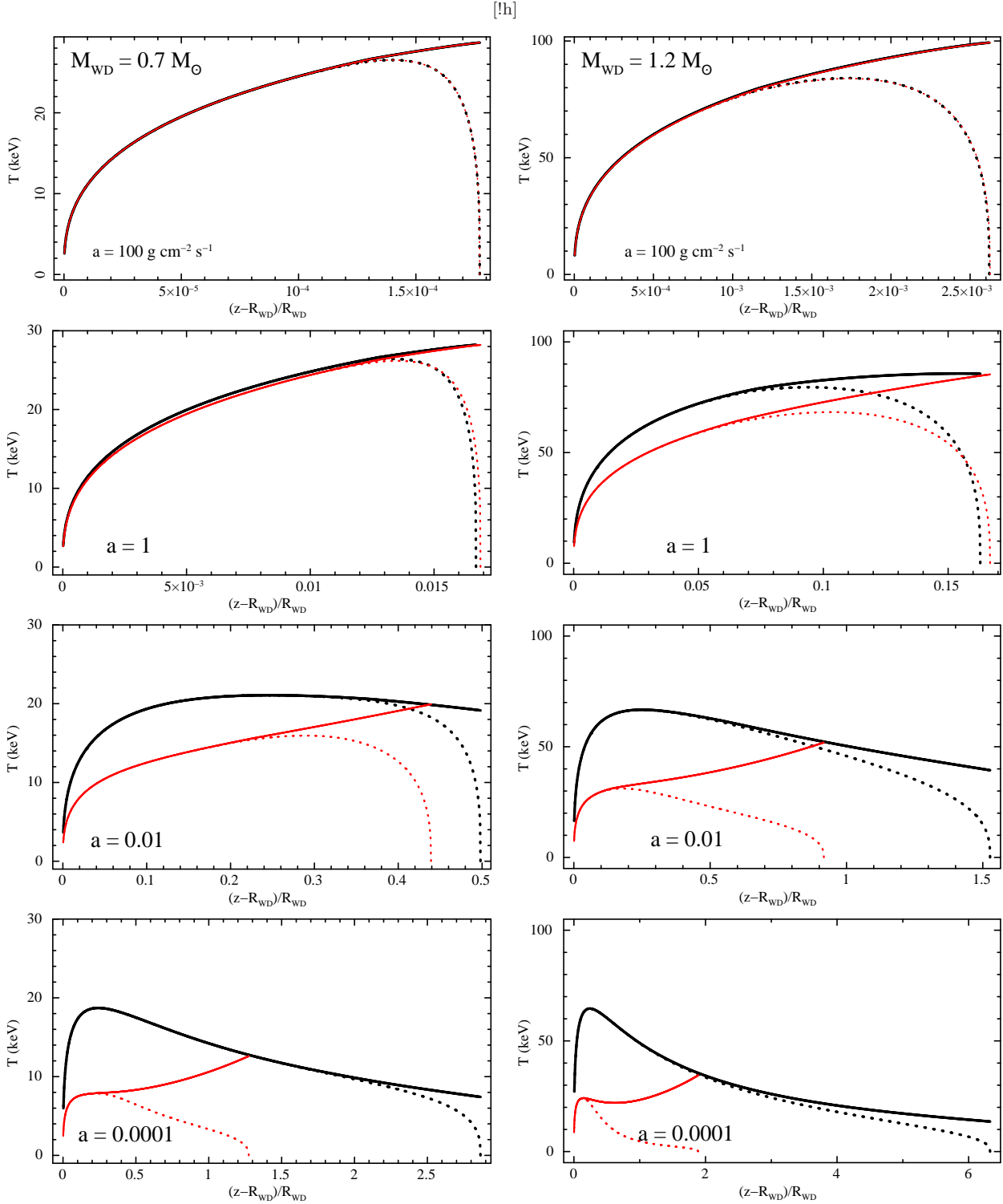


Figure 4. Averaged (solid) and electron (dotted) temperature distributions of the cylindrical (black) and dipolar (red) PSACs for the WD mass of 0.7 (left columns) and 1.2 (right columns) M_{\odot} and a of 0.0001, 0.01, 1, $100 \text{ g cm}^{-2} \text{ s}^{-1}$ from bottom to top panels.

the dipolar geometry because the density is smaller than in the cylindrical geometry especially at around the top of the PSAC, which delays accomplishment of the equipartition.

3.3 Dependency on the metal abundance

We investigated influence of metal abundance on the PSAC structure as well as the specific accretion rate and the WD mass. In figure 7 we show the PSAC structures by assuming 0.1, 0.5, 1.0 and 2.0 Z_{\odot} with the cylindrical or dipolar

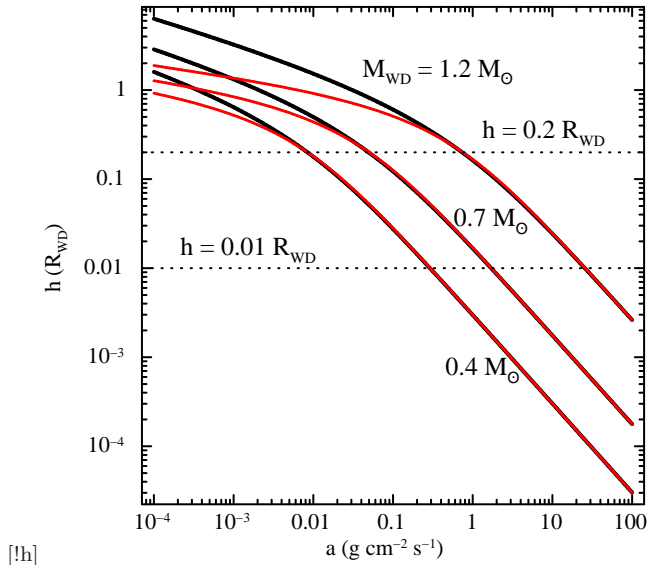


Figure 5. The PSAC heights for the 0.4, 0.7 and $1.2 M_{\odot}$ WDs as a function of the specific accretion rate. Black and red lines show the cylindrical and dipolar cases, respectively. The horizontal dotted line represents 20% of the WD radius, which defines the threshold specific accretion rate. Note that the heights in this figure are normalized by each WD radii.

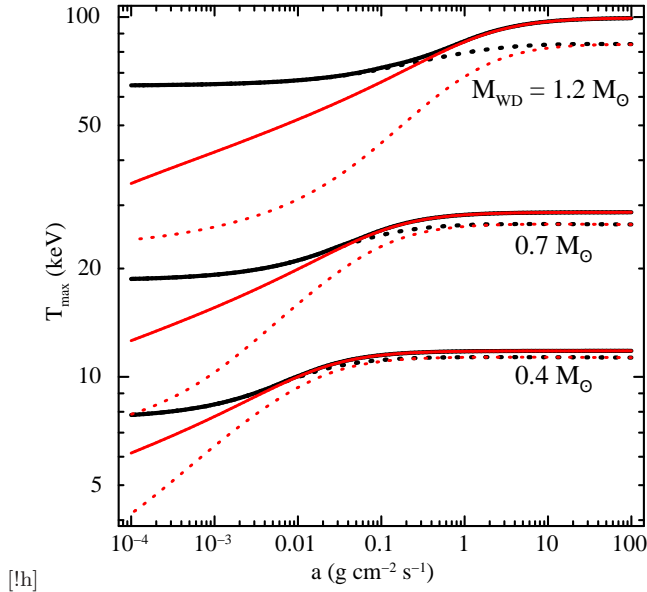


Figure 6. Averaged (solid) and electron (red) maximum temperatures relating the specific accretion rate for 0.4, 0.7 and $1.2 M_{\odot}$ of the WDs. Black and red lines show the cylindrical and dipolar PSACs, respectively.

geometries. The top panel of figure 7 displays examples of the cylinder PSACs on the $0.7 M_{\odot}$ WD. Note that, although cylindrical geometry is assumed, the profiles can be regarded as those of the dipolar PSACs, because the assumed specific accretion rate is sufficiently high. The middle and bottom panels show the temperature distributions for cylindrical and dipolar PSACs on the $0.7 M_{\odot}$ WD, respectively.

These results mean that the influence of the metal abundance on the PSAC structure is even less significant than

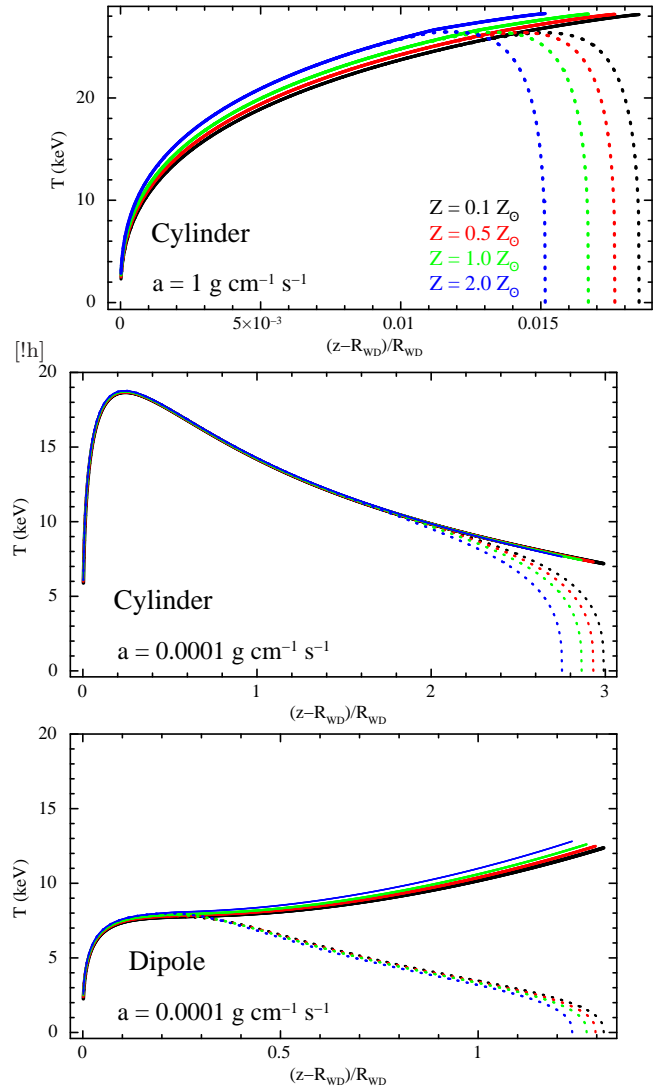
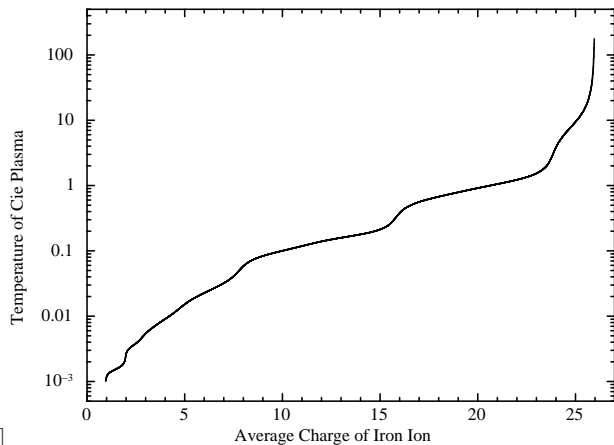


Figure 7. Averaged (solid) and electron (dotted) temperature distributions for abundances of 0.1 (black), 0.5 (red), 1.0 (green) and 2.0 (blue) times the solar abundance. Top panel shows that the distributions for the cylindrical PSAC and $a = 1 \text{ g cm}^{-2} \text{ s}^{-1}$, which is almost identical to that of the dipolar PSACs with the same specific accretion rates. The middle and bottom panels show the distributions for the cylindrical and dipolar PSACs with $a = 0.0001 \text{ g cm}^{-2} \text{ s}^{-1}$. The WD mass of $0.7 M_{\odot}$ is adopted.

that of the specific accretion rate. Moreover, since the abundances of IPs are generally in the range from 0.1 to 0.6 times of solar abundance (Yuasa et al. 2010), the influence of the metal abundance on the PSAC structure is limited. However, the metal abundance significantly affects X-ray spectrum, especially line spectra (see section 4). Therefore, we remain the metal abundance as an input parameter in the following section.

4 X-RAY SPECTRA

In this section, we calculate X-ray spectra emitted from the PSACs using the temperature and density distributions calculated in section 3.

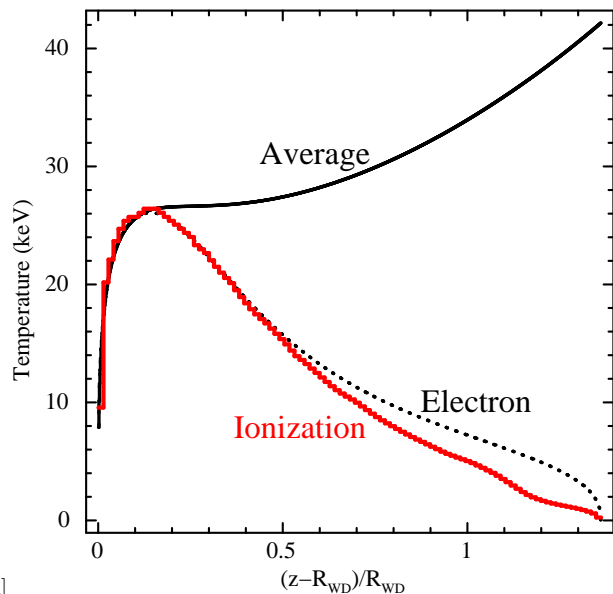


[lh]
Figure 8. Relation between the average charge of iron ion and the ionization temperature calculated by the SPEX.

4.1 Spectral calculation method

In order to calculate the spectra, the PSAC is divided into evenly spaced one hundred segments within each of which the physical quantities can be regarded as constant, and then the one hundred partial spectra are summed up. Spectra emitted from each segments are calculated with one temperature plasma emission models in SPEX package (Kaastra et al. 1996).

In calculating the partial X-ray spectra, we need to take into account the non-equilibrium between ions and electrons for part of the PSAC and hence used the following two X-ray spectrum models; one is the Cie (Collisional ionization equilibrium) model and the other is Neij (Non-Equilibrium Ionization Jump model; Kaastra & Jansen (1993)) model, both included in the SPEX package. In general, equipartition between ions and electrons and ionization state of the ions in plasma reach thermal equilibrium if the product of the electron number density and the elapsed time since the shock becomes greater than $n_{et} > 10^{12} \text{ cm}^{-3} \text{ s}$ (Masai 1984). Accordingly, for the PSAC segments at which $n_{et} > 10^{12} \text{ cm}^{-3}$, the Cie model is adopted where the input temperature is common among the ions, the electrons and the ionization. For the PSAC segments at which $n_{et} < 10^{12} \text{ cm}^{-3}$, on the other hand, the Neij model is adopted, which is characterized by the three parameters nt , T_{ion} and T . The T_{ion} and T are initial ionization temperature and initial common temperature of the ions and the electrons, respectively. Thus, the Neij model can only treat the case that the ions and the electrons share a common kinematical temperature, whereas our hydrodynamical model predicts that they in real have different temperatures near the top of the PSAC. However, since the ionization process is governed by electron impacts to the ions, we adopt the electron temperature for T . T_{ion} is used as the ionization temperature that is common among all elements reaching the start points of each segment. The initial ionization temperature T_{ion} of a segment is evaluated from the average charge of iron ion achieved by the previous PSAC segment through a relation between the average charge of iron ion and the ionization temperature, which is calculated by the SPEX (figure 8). Only for the first segment laying on the top of the PSAC, T_{ion} is set to 0.002 keV, the limit of the Neij model.



[lh]
Figure 9. Averaged (black solid), electron (black dotted) and ionization (red solid) temperatures for the case $M_{\text{WD}} = 1.2 M_{\odot}$ and $a = 0.001 \text{ g cm}^{-2} \text{ s}^{-1}$.

Figure 9 shows the ionization temperature calculated by the method defined above. For this figure $M_{\text{WD}} = 1.2 M_{\odot}$ and $a = 0.001 \text{ g cm}^{-2} \text{ s}^{-1}$ are adopted where the non-equipartition are prominent (figure 4). The ionization temperature does not catch up that of electron in about 70% of the PSAC from its top. We note, however, that the density of the segments in the ionization non-equilibrium area is smaller than those in equilibrium by one or two orders magnitudes, which implies that the ionization non-equilibrium does not affect the resultant total X-ray spectrum significantly.

4.2 X-ray spectra

In figure 10, resultant spectra are shown for the cases $M_{\text{WD}} = 0.7 M_{\odot}$, $Z = Z_{\odot}$, $a = 100, 1, 0.01$ and $0.0001 \text{ g cm}^{-2} \text{ s}^{-1}$, as well as ratios of them to that of $a = 1 \text{ g cm}^{-2} \text{ s}^{-1}$. The results are shown both for the cylinder and dipole geometries. In a higher specific accretion rate domain, the flux increases in proportion to the specific accretion rate. Since the profiles of the temperature and density distributions resemble each other between the two PSAC geometries in the cases of $a = 1$ and $100 \text{ g cm}^{-2} \text{ s}^{-1}$, their spectral shapes are almost identical. However, at He-like iron $K\alpha$ line ($\sim 6.7 \text{ keV}$), the spectral shapes of the $a = 1$ and $100 \text{ g cm}^{-2} \text{ s}^{-1}$ cases are considerably different in both geometries. This is because the density of PSAC reaches the critical density of iron $\sim 10^{18} \text{ cm}^{-3}$ between $a = 1$ and $100 \text{ g cm}^{-2} \text{ s}^{-1}$ and relative intensities of the He-like $K\alpha$ triplet alter with the density (figure 11). On the other hand, the spectral shapes in the cases of $a = 0.01$ and $0.0001 \text{ g cm}^{-2} \text{ s}^{-1}$ clearly deviate from that of $a = 1 \text{ g cm}^{-2} \text{ s}^{-1}$ for both PSAC geometries, because the temperature of the PSACs are significantly reduced as the specific accretion rate becomes lower (figure 4 and 6). Change of ratios of H- and He-like iron $K\alpha$ lines (figure 11) and

deformation of the continuum above 10 keV energy bands are especially prominent, and observationally important because the energy bands where these two phenomena emerge are hard to be influenced by complex and heavy absorbers generally detected in the X-ray spectra of IPs. These spectral changes with the specific accretion rate is larger for the dipolar PSAC, and the spectrum of the dipolar PSAC is softer than that of the cylindrical at the same specific accretion rate. Since these deformations emerge in lower specific accretion rate systems, the specific accretion rate should be considered as an important parameter in order to extract physical parameters such as WD masses from X-ray spectra. At the same time, the spectral deformation potentially enables us to measure the specific accretion rate with X-ray spectroscopy which may give geometrical information of the height of PSAC, the accreting area on the WD surface and shape of the PSAC.

Note that influence of the ionization non-equilibrium on X-ray spectrum is not significant because of the low density of such PSAC domains for both geometries, although that effect is properly considered in this work. For example, we obtained a result that the dipolar PSAC with $M_{\text{WD}} = 0.7 M_{\odot}$, $a = 0.0001 \text{ g cm}^{-2} \text{ s}^{-1}$ and $Z = Z_{\odot}$ at which parameters the non-equilibrium effect manifests itself prominently, shows a spectrum more intense by about 4% around 0.7 keV and less intense by 0.01–0.02% between 10 and 100 keV at most than the ionization equilibrium spectrum. At the energy around 0.7 keV, an iron L line forest is enhanced due to the ionization non-equilibrium effect because the ionization does not proceed compared with the equilibrium case. On the other band, bremsstrahlung radiation dominating over the latter energy band ($> 10 \text{ keV}$) is weaker for the non-equilibrium model because of low electron temperature. Even, in the energy band above 5 keV that is important for the study of the PSAC for most mCVs (Ezuka & Ishida 1999), the difference is only about 0.2%, which does not matter for the current observation quality.

The problem of the discrepancy of the WD mass measurement (§1) may be resolved if we treat the specific accretion rate as a free model parameter. The X-ray spectrum of the PSAC is softer than that of the standard model in the domain $a < a_{\text{crit}}$, which makes the resultant WD mass more massive. We will verify this possibility by applying our model to observations in the forthcoming paper.

5 SUMMARY

We calculated the density and temperature distributions of the PSAC in IPs by taking into account dependence on the specific accretion rate, the dipolar magnetic geometry, non-equipartition between electrons and ions, ionization non-equilibrium, and release of the gravitational potential with the form proportional to r^{-1} . In particular, the specific accretion rate is floated over the wide range between 0.0001 to $100 \text{ g cm}^{-2} \text{ s}^{-1}$. This is the first comprehensive PSAC model that all these factors are fully taken into account. With the density and temperature profiles, we constructed a spectral model by dividing the PSAC radially into a hundred segments, and by integrating the spectrum from each segment calculated with the SPEX package. In our modeling, the free

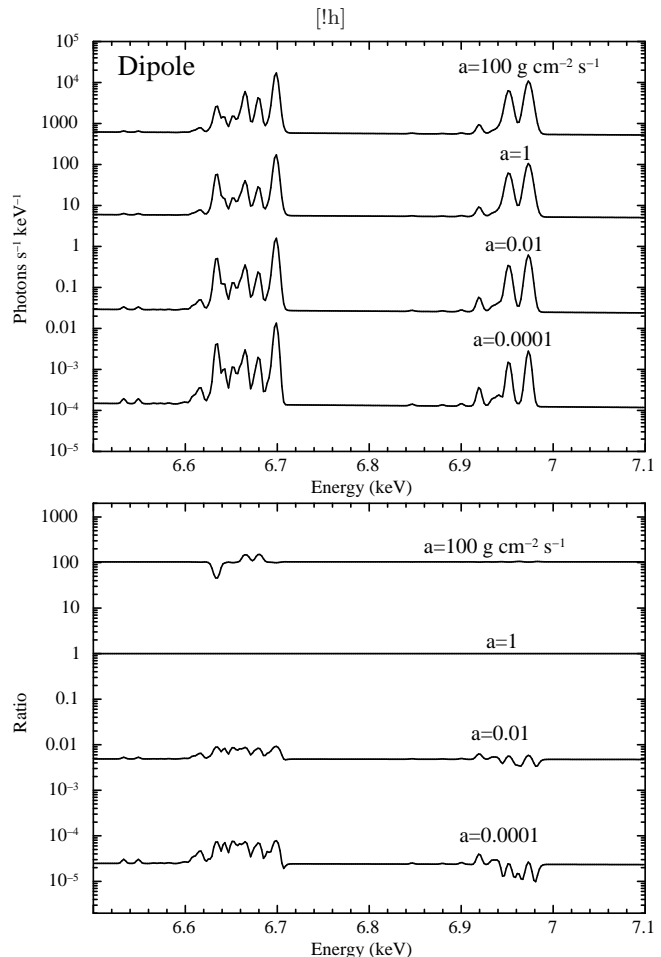


Figure 11. Iron $K\alpha$ lines (top panel) emitted from dipolar PSACs for $M_{\text{WD}} = 0.7 M_{\odot}$, and $a = 100, 1, 0.01$ and $0.0001 \text{ g cm}^{-2} \text{ s}^{-1}$. The ratio to the iron $K\alpha$ lines with $a = 1 \text{ g cm}^{-2} \text{ s}^{-1}$ (bottom panel). Abundance is assumed to be one solar.

parameters are the WD mass, the specific accretion rate and the metal abundance.

We found difference of the specific accretion rate significantly alters the profiles of the density and temperature distributions. As long as the specific accretion rate is high enough, the density and temperature distributions of our modeling are consistent with those of the present standard model. There is, however, a critical specific accretion rate below which the profiles of the density and temperature distributions significantly deviate from those of the standard model. The standard model is no longer valid, if the specific accretion rate is below the critical value a_{crit} , which is about 1 and $30 \text{ g cm}^{-2} \text{ s}^{-1}$ for the 0.7 and $1.2 M_{\odot}$ WD, respectively, or when the height of the PSAC reaches about 1% of the WD radius. In addition, the profiles become different between the cylindrical and the dipolar geometries. The temperature profile shows the peak in the middle of the PSAC for the cylindrical geometry whereas that for the dipole geometry declines toward the WD surface more rapidly than that of the standard model. Since the WD radius reduces for more massive WD, the critical specific accretion rate is lower for the IPs holding the less massive WD.

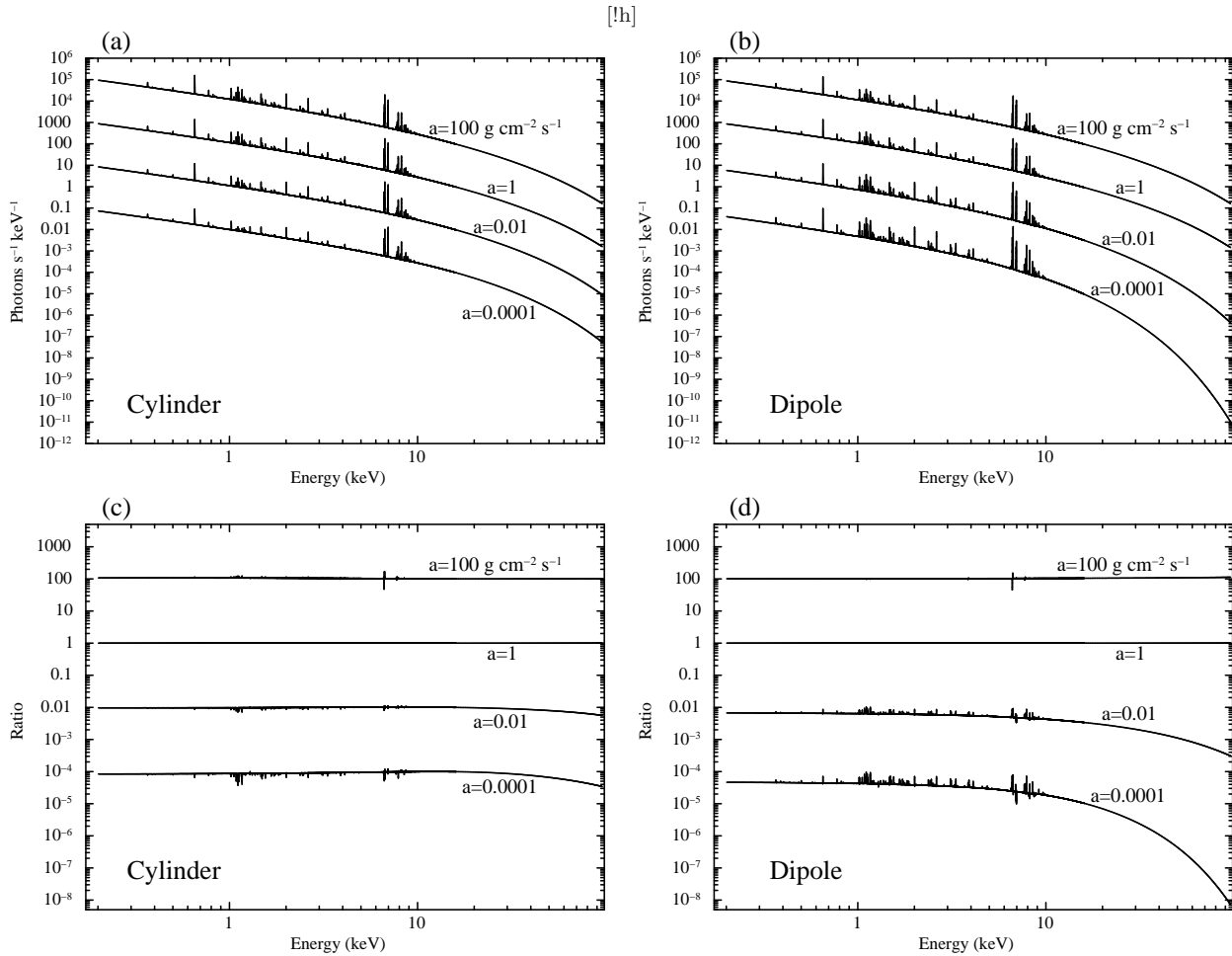


Figure 10. X-ray spectra emitted from (a) cylindrical and (b) dipolar PSACs for $M_{\text{WD}} = 0.7 M_{\odot}$, and $a = 100, 1, 0.01$ and $0.0001 \text{ g}^{-1} \text{ cm}^{-2} \text{ s}^{-1}$. The spectral ratios to the spectrum with $a = 1 \text{ g}^{-1} \text{ cm}^{-2} \text{ s}^{-1}$ for the (c) cylindrical and (d) dipolar. Abundance is assumed to be one solar.

The profiles of the density and temperature distributions significantly changed with the decrease of the specific accretion rate below the critical value, and mutual difference of the profiles between the two geometries is also enhanced. The non-equipartition between electrons and ions are significant in lower density domains, and hence, the non-equipartition is more significant for the dipolar PSAC. With the low specific accretion rate of $0.0001 \text{ g cm}^{-2} \text{ s}^{-1}$ the non-equipartition domain occupies 80% of the PSAC from its top for IPs holding a $0.7 M_{\odot}$ WD. We also investigated the influence of the metal abundance, and found that it hardly influences the PSAC structure between 0.1 and 2 solar abundance which covers the entire IP population so far observed.

We calculated the X-ray spectra with the density and temperature distributions and found that the X-ray spectra depend on the specific accretion rate. The X-ray spectra with the higher specific accretion rate than the critical value is almost constant except for the He-like iron $K\alpha$ emission line due to the density dependence of the He-like triplet of the iron $K\alpha$ line. When the specific accretion rate is smaller than the critical value, since the temperature in the PSAC reduces, the X-ray spectra soften, which is more prominent for the dipolar PSAC. Specifically, the continuum component above 10 keV and the ratio of H-like line to that of

He-like reduces as the specific accretion rate decreases. The ionization non-equilibrium is not significant on X-ray spectra because of lower density than in equilibrium domain by a few orders of magnitudes.

ACKNOWLEDGEMENT

The authors would like to thank Prof. Ohashi T., Prof. Masai K. and Associate Prof. Ishisaki T. for their very useful comments.

REFERENCES

- Aizu K., 1973, PThPh, 49, 1184
- Allan A., Hellier C., Beardmore A., 1998, MNRAS, 295, 167
- Beuermann K., Reinsch K., 2008, A&A, 480, 199
- Brunschweiler J., Greiner J., Ajello M., Osborne J., 2009, A&A, 496, 121
- Canalle J. B. G., Saxton C. J., Wu K., Cropper M., Ramsay G., 2005, A&A, 440, 185

- Casares J., Mouchet M., Martinez-Pais I. G., Harlaftis E. T., 1996, MNRAS, 282, 182
- Cropper M., Ramsay G., Wu K., 1998, MNRAS, 293, 222
- Cropper M., Wu K., Ramsay G., Kocabiyik A., 1999, MNRAS, 306, 684
- Eracleous M., Halpern J., Patterson J., 1991, ApJ, 382, 290
- Ezuka H., Ishida M., 1999, ApJS, 120, 277
- Frank J., King A., Raine D., 1992, *apa.book*,
- Fujimoto R., Ishida M., 1997, ApJ, 474, 774
- Hachisu I., Kato M., 2007, ApJ, 662, 552
- Hayashi T., Ishida M., Terada Y., Bamba A., Shionome T., 2011, PASJ, 63, 739
- Hōshi R., 1973, PThPh, 49, 776
- Imamura J. N., Durisen R. H., 1983, ApJ, 268, 291
- Itoh K., Okada S., Ishida M., Kunieda H., 2006, ApJ, 639, 397
- Kaastra J. S., Jansen F. A., 1993, A&AS, 97, 873
- Kaastra, J. S., Mewe, R., & Nieuwenhuijzen, H. 1996, *UV and X-ray Spectroscopy of Astrophysical and Laboratory Plasmas*, 411
- Landi R., Bassani L., Dean A. J., Bird A. J., Fiocchi M., Bazzano A., Nousek J. A., Osborne J. P., 2009, MNRAS, 392, 630
- Masai K., 1984, Ap&SS, 98, 367
- Nauenberg M., 1972, ApJ, 175, 417
- Patterson J., 1979, ApJ, 234, 978
- Ramsay G., Potter S., Cropper M., Buckley D. A. H., Harrop-Allin M. K., 2000, MNRAS, 316, 225
- Saxton C. J., Wu K., Cropper M., Ramsay G., 2005, MNRAS, 360, 1091
- Saxton C. J., Wu K., Canalle J. B. G., Cropper M., Ramsay G., 2007, MNRAS, 379, 779
- Schure K. M., Kosenko D., Kaastra J. S., Keppens R., Vink J., 2009, A&A, 508, 751
- Spitzer L., 1962, *pfig.book*
- Suleimanov V., Revnivtsev M., Ritter H., 2005, A&A, 435, 191
- Woelk U., Beuermann K., 1996, A&A, 306, 232
- Wong K.-W., Sarazin C. L., 2009, ApJ, 707, 1141
- Wu K., Chanmugam G., Shaviv G., 1994, ApJ, 426, 664
- Wynn G. A., King A. R., Horne K., 1997, MNRAS, 286, 436
- Yuasa T., Nakazawa K., Makishima K., Saitou K., Ishida M., Ebisawa K., Mori H., Yamada S., 2010, A&A, 520, A25